ADVANCED FUNCTIONAL MATERIALS
www.afm-journal.de

Materials Views
www.MaterialsViews.com

Pyrite-Based Bi-Functional Layer for Long-Term Stability and High-Performance of Organo-Lead Halide Perovskite Solar Cells

*Bonkee Koo, Heesuk Jung, Minwoo Park, Jae-Yup Kim, Hae Jung Son, Jinhan Cho, and Min Jae Ko**

Organo-lead halide perovskite solar cells (PSCs) have received great attention because of their optimized optical and electrical properties for solar cell applications. Recently, a dramatic increase in the photovoltaic performance of PSCs with organic hole transport materials (HTMs) has been reported. However, as of now, future commercialization can be hampered because the stability of PSCs with organic HTM has not been guaranteed for long periods under conventional working conditions, including moist conditions. Furthermore, conventional organic HTMs are normally expensive because material synthesis and purification are complicated. It is herein reported, for the first time, octadecylamine-capped pyrite nanoparticles (ODA-FeS_2 NPs) as a bi-functional layer (charge extraction layer and moisture-proof layer) for organo-lead halide PSCs. FeS_2 is a promising candidate for the HTM of PSCs because of its high conductivity and suitable energy levels for hole extraction. A bi-functional layer based on ODA-FeS_2 NPs shows excellent hole transport ability and moisture-proof performance. Through this approach, the best-performing device with ODA-FeS_2 NPs-based bi-functional layer shows a power conversion efficiency of 12.6% and maintains stable photovoltaic performance in 50% relative humidity for 1000 h. As a result, this study has the potential to break through the barriers for the commercialization of PSCs.

1. Introduction

Perovskite solar cells (PSCs) are emerging as one of the promising next-generation photovoltaic devices because of several advantages such as ease of fabrication, low cost, and high efficiency.[1–5] Miyasaka and co-workers introduced organic–inorganic hybrid alkylammonium lead halide perovskites (R-NH_3PbX_3, X = Cl, Br, I) as an inorganic sensitizer in liquid-type dye-sensitized solar cells.[6] However, the performance of this solar cell was significantly degraded because the perovskites were dissolved in a polar liquid electrolyte. Park and co-workers reported all-solid-state PSCs, which increased the power conversion efficiencies (PCEs) up to 9.7%, using 2,2′,7,7′-tetrakis(*N*,*N*-di-*p*-methoxyphenylamine)9,9′-spirobifluorene (spiro-OMeTAD).[7] Recently, the PCE of PSCs with solid junctions has rapidly improved and a certified PCE of 21.0% was reported by the National Renewable Energy Laboratory (NREL) in the records of the best research cell efficiency.[8–13]

Although PSCs employing organic hole transport materials (HTMs) such as spiro-OMeTAD have demonstrated excellent photovoltaic performance, there are still enormous drawbacks such as cost and hygroscopic p-type dopants for enhanced conductivity, leading to moisture penetration. The cost of high purity spiro-OMeTAD is more than ten times that of gold or platinum because materials synthesis and purification of spiro-OMeTAD is very complicated.[14] Furthermore, moisture can easily permeate through the spiro-OMeTAD layer since the lithium-bis(trifluoromethane)sulfonamide (Li-TFSI) in spiro-OMeTAD is hygroscopic.[15] Perovskites become unstable when they are exposed to polar solvents such as water. This could lead to degradation under humid conditions within several minutes, resulting in the production of toxic lead compounds.[16,17]

Alternative organic materials such as (poly-[[9-(1-octylnonyl)-9H-carbazole-2,7-diyl]-2,5-thiophenediyl-2,1,3-benzothiadiazole-4,7-diyl-2,5-thiophenediyl]) (PCDTBT), poly-[2,1,3-benzothiadiazole-4,7-diyl[4,4-bis(2-ethylhexyl)-4H-cyclopenta[2,1-*b*:3,4-*b*′]-dithiophene-2,6-diyl]] (PCPDTBT), poly-3-hexylthiophene (P3HT), and poly-triarylamine (PTAA) are also used for HTMs.[17] However, these materials are also expensive and

B. Koo, H. Jung, Dr. M. Park, Dr. J.-Y. Kim, Dr. H. J. Son, Dr. M. J. Ko
Photo-electronics Hybrids Research Center
Korea Institute of Science and Technology (KIST)
Seoul 02792, Korea
E-mail: mjko@kist.re.kr
B. Koo, Prof. J. Cho
Department of Chemical and Biological Engineering
Korea University
Anam-dong, Seongbuk-gu, Seoul 02841, Korea
Prof. M. Park
Department of Chemical and Biological Engineering
Sookmyung Women's University
Seoul 04310, Korea
Prof. H. J. Son, Prof. M. J. Ko
Green School
Korea University
145, Anam-ro, Seongbuk-gu, Seoul 02841, Korea
Prof. M. J. Ko
KU-KIST Graduate School of Converging Science and Technology
Korea University
Seoul 02792, Korea

DOI: 10.1002/adfm.201601119

need to be mixed with ionic additives for higher hole mobility. Considering this, the limitations of organic HTM could be an obstacle to future commercialization of perovskite photovoltaics.

On the contrary, inorganic p-type semiconductors appear to be an ideal choice because of their low cost, stability, ease of synthesis, and high mobility without ionic additives.[18,19] Kamat and co-workers reported that an inexpensive and solution-processable inorganic p-type material, copper iodide (CuI), based perovskite photovoltaics exhibited a PCE of 6%.[20] More recently, Nazeeruddin and co-workers introduced copper thiocyanate (CuSCN) as an inorganic hole conductor in PSCs, and the device exhibited a high PCE of above 12%.[21] However, it is conjectured that their approaches might not guarantee the long-term stability of perovskites. Generally, the ionic exchange reaction could occur between the Cu of inorganic HTMs and Pb in perovskite absorbers.[22–25]

In order to overcome the disadvantages of inorganic HTMs, ligand-passivated pyrite nanoparticles (FeS_2 NPs) were used in the hole transporting layer of PSCs. FeS_2 is one of the most promising candidates for the HTM of PSCs because FeS_2 has advantages such as earth abundance, non-toxicity, high charge-carrier mobility, and appropriate energy levels for hole extraction.[26–31] However, the hydrophilicity of FeS_2 has been an obstacle for use in the upper HTM layer of PSCs. Therefore, we synthesized FeS_2 NPs with long alkyl chain ligands such as octadecylamine (ODA) to facilitate their use as the upper layer of the perovskite absorber. Ligand-modified NPs have been known as a facile method to provide hydrophobicity to NPs.[32–35] Herein, ODA molecules with long hydrophobic alkyl chains were used to modify the hydrophilic surfaces of FeS_2 into hydrophobic surfaces. As a result, ODA-capped FeS_2 NPs (ODA-FeS_2 NPs) based HTM layer was deposited on the perovskite layer and exhibited large water contact angles >110°. Compared to spiro-OMeTAD, the HTM layer based on ODA-FeS_2 NPs were more hydrophobic. Furthermore, the long alkyl chain of ODA prevented the ionic exchange between inorganic HTM and the perovskite absorber, which contributed to the chemical stability of ODA-FeS_2 NPs.

We also demonstrated that ODA-FeS_2 NPs function as an efficient charge transporter. The ODA-FeS_2 NPs layer exhibited excellent conductivity, one order of magnitude higher than that of pristine spiro-OMeTAD. The best-performing PSC with ODA-FeS_2 NPs-based HTM showed a high PCE of 12.56% and maintained its photovoltaic performance for 1000 h under 50% relative humidity (RH). As a result, we verify that ODA-FeS_2 NPs-based HTM acts efficiently as a bi-functional layer (charge extraction layer and moisture-proof layer) through its high conductivity and its ability to act as a moisture barrier.

2. Results and Discussion

2.1. Synthesis and Characterization of ODA-FeS_2 Nanostructures

We synthesized ODA-FeS_2 NPs using a hot injection method reported by Puthussery.[28] **Figure 1**a shows the high-resolution transmission electron microscopy (HR-TEM) image of ODA-FeS_2 NPs. Even at higher concentrations, ODA-FeS_2 NPs have a narrow size distribution without aggregation or impurities. The inset in Figure 1a also shows the ODA-FeS_2 NP, and the lattice distance (d) is 2.7 Å, attributed to the [002] crystalline plane of FeS_2. As shown in Figure 1b, X-ray diffraction (XRD) data also indicated that all the reflection peaks could be indexed to a single phase of ODA-FeS_2 NPs without other peaks from impurities such as marcasite, pyrrhotite, or troilite.[36] To investigate the atomic ratio of the pyrite, we performed X-ray photoelectron spectroscopy (XPS). As shown in Figure 1c, the two resolved peaks at 711.8 and 726.6 eV correspond to Fe $2p_{3/2}$ and Fe $2p_{1/2}$, respectively. In Figure 1d, the binding energy peaks of S located at 162.6 and 163.7 eV, attributed to the S $2p_{3/2}$ and S $2p_{1/2}$, respectively, are consistent with the binding energy of sulfur in pyrite.[37,38] These results indicate that the sulfur to iron atomic ratio was about 2, which is identical to pyrite. As a result, we demonstrated that the ODA-FeS_2 NPs could be synthesized without impurities and precisely controlled via the hot injection method.

2.2. Characterization of ODA-FeS_2 NPs-Based HTM Layer

Typically, the HTM layer is located on the top of the perovskite light absorber. The perovskite structure is degraded when it contacts a polar solvent such as water. Thus, an HTM with hydrophobicity is required to prevent the decomposition of perovskite. To demonstrate the hydrophobicity of ODA-FeS_2 NPs, static contact angles were measured. For comparison, a spiro-OMeTAD layer was also prepared. As shown in **Figure 2**a, the contact angle of a water droplet on the surface of spiro-OMeTAD film was 77.1°. On the other hand, that of the HTM film with ODA-FeS_2 NPs was 112.9° because of the hydrophobic nature of the ODA ligand. As a result, the differences in wettability between the film based on ODA-FeS_2 NPs and spiro-OMeTAD prove the possibility of ODA-FeS_2 NPs as a moisture-proof layer for perovskite absorber. Furthermore, we studied the morphology of the ODA-FeS_2 nanostructured film using scanning electron microscopy (SEM) and atomic force microscopy (AFM). As shown in Figure 2b, ODA-FeS_2 NPs were deposited uniformly and densely on the perovskite substrates without pinholes by the spray-coating method. Figure 2c shows that the surface roughness of the film was ≈5.817 nm. Thus, the results reveal that a spray-coated film based on ODA-FeS_2 NPs has a pinhole free surface, which contributes to the protection of the perovskite absorber.

In order to demonstrate the possibility of using ODA-FeS_2 NPs as an HTM, we measured the conductivity of ODA-FeS_2 nanostructured thin film. A standard four-pin probe measurement was used to confirm the conductivity of ODA-FeS_2 NPs-based HTM. ODA-FeS_2 nanostructured thin film has a conductivity of 2.78×10^{-4} S cm^{-1}, one order of magnitude higher than that of the pristine spiro-OMeTAD (2×10^{-5} S cm^{-1}). Even when the FeS_2 NPs were capped by long alkyl chain ligands, the ODA-FeS_2 nanostructured film could perform as a charge transporting layer. In addition, C-AFM was employed to study the charge carrier behavior in the thin film based on the ODA-FeS_2 NPs. Figure 2d shows that the current flow through the ODA-FeS_2 nanostructured HTM layer is randomly distributed.

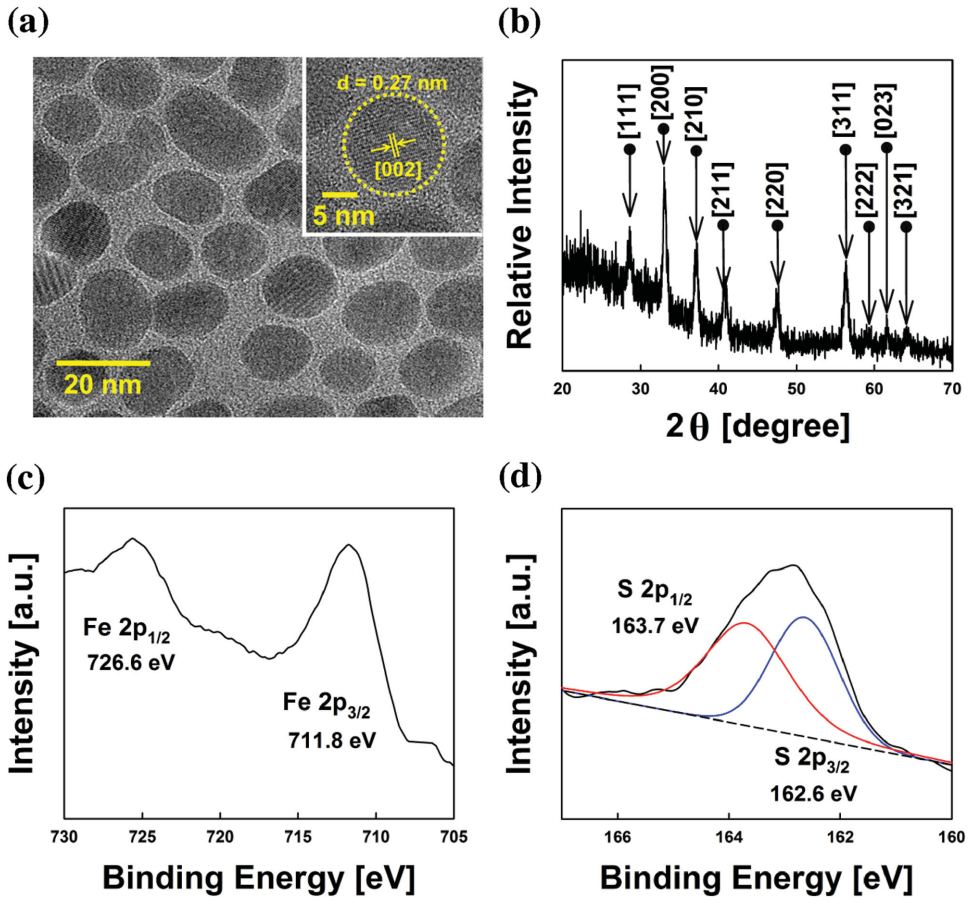

Figure 1. Synthesis and characterization of ODA-FeS_2 NPs. a) High-resolution TEM image of ODA-FeS_2 NPs. The inset shows 10 nm ODA-FeS_2 NPs and the lattice fringe attributed to the [002] plane of pyrite. b) XRD pattern of FeS_2 NPs stabilized by ODA. XPS spectra of c) Fe 2p and d) S 2p.

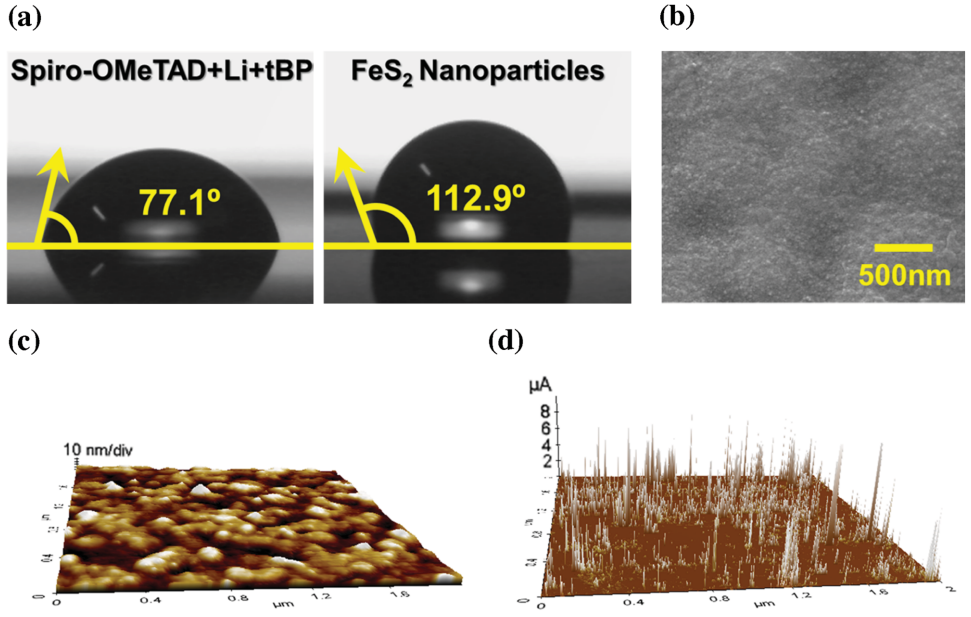

Figure 2. Characterization of films based on hole transporting materials. a) Measurement of static contact angles of water droplets on the surface of spiro-OMeTAD (left image) and film based on ODA-FeS_2 NPs (right image). b) SEM planar view of ODA-FeS_2 NPs-based film, c) AFM topographic image, and d) CS-AFM image of the ODA-FeS_2 NPs-based film prepared by spray-coating (solution concentration: 0.5 mg mL^{-1}).

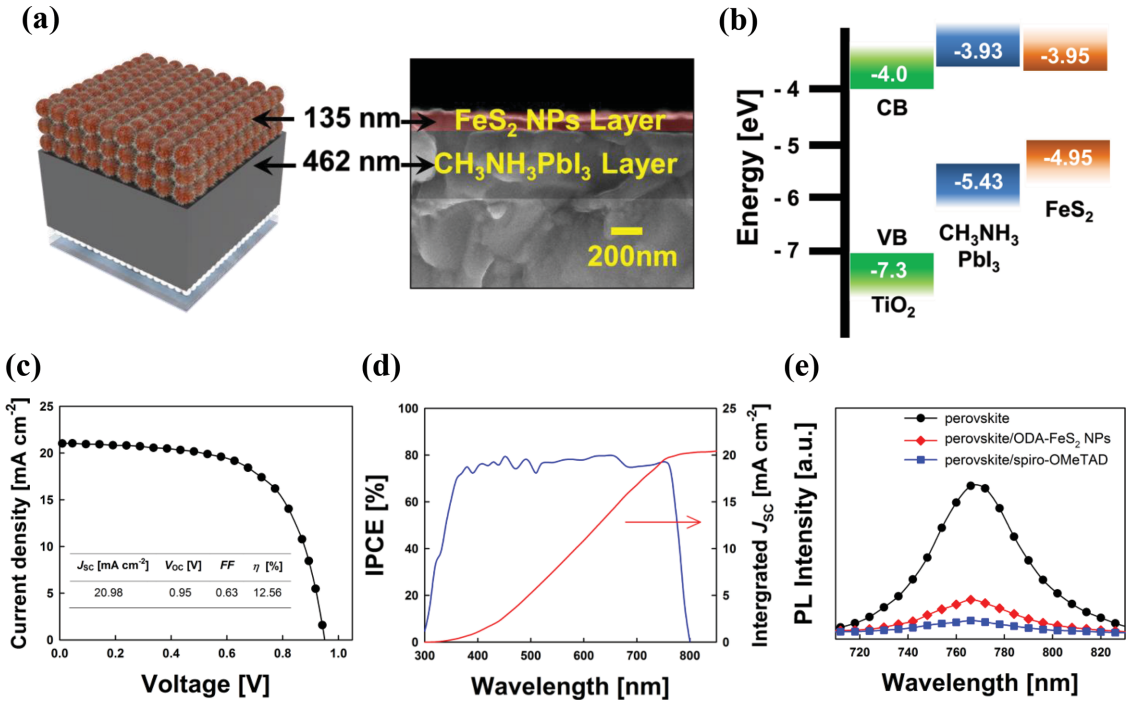

Figure 3. a) Device architecture and cross-sectional SEM image of the perovskite solar cells (PSCs) with ODA-FeS_2 NPs-based hole transporting layer (HTL). b) Schematic of an energy diagram of the TiO_2/$CH_3NH_3PbI_3$/HTM based on ODA-FeS_2 NPs. c) Photocurrent density–voltage (*J–V*) curve under 100 mW cm^{-2} illumination (AM 1.5G). d) Incident photon to current efficiency (IPCE) spectrum of the highest-performing PSC comprising ODA-FeS_2 NPs-based HTM (blue line). The integrated product of the IPCE curve with an AM 1.5G spectrum (red line). e) Steady-state photoluminescence (PL) spectra of the bare perovskite, perovskite absorber/ODA-FeS_2 NPs based HTL, and perovskite absorber/spiro-OMeTAD.

The charge carriers drift in the electric field through the most favorable diffusion paths to form channels with high electrical conductivity.[39] We further investigated the hole mobility of ODA-FeS_2 nanostructured thin film, bulk FeS_2. ODA-FeS_2 NPs based hole transporting film has the hole mobility of 0.0312 cm^2 V^{-1} S^{-1}, which is one order of magnitude higher than that of spiro-OMeTAD. The hole mobility of bulk FeS_2 film is 293 cm^2 V^{-1} S^{-1}. Compared to spiro-OMeTAD, ODA capped FeS_2 NPs based HTM has the advantage of higher mobility. These results demonstrate that a bi-functional layer based on ODA-FeS_2 NPs could act as both a hole transportation and moisture-proof layer in perovskite solar cells.

2.3. Device Structure and Photovoltaic Performance of PSCs with ODA-FeS_2 HTM

Figure 3a shows a schematic of the device structure and the cross-sectional SEM image of the PSC with an HTM layer based on ODA-FeS_2 NPs. The ODA-FeS_2 NPs-based HTM layer has a thickness of 135 nm and is completely covered on the $CH_3NH_3PbI_3$ layer without any pinholes. Therefore, we conjecture that the layer based on ODA-FeS_2 NPs could block direct contact between the $CH_3NH_3PbI_3$ and the Au cathode. As shown in Figure 3b, the energy level diagram of the components proves that FeS_2 has a suitable band position for hole extraction in PSCs.[30] To demonstrate the ability of the HTM based on ODA-FeS_2 NPs for hole extraction, we prepared PSCs that have a fluorine-doped tin oxide (FTO)/TiO_2 blocking layer/mesoporous TiO_2 layer/$CH_3NH_3PbI_3$/ODA-FeS_2 NPs/Au components. The fabrication process of PSC with ODA-FeS_2 NPs-based HTM is shown in Figure S1 (Supporting Information). For comparison, reference cells with spiro-OMeTAD were also prepared under the same condition.

Figure 3c shows the photovoltaic properties (*J–V* curves) of the highest-performing device with ODA-FeS_2 NPs-based HTM. As shown in the inset of Figure 3c, the best performing solar cells with HTM based on ODA-FeS_2 NPs exhibited a short circuit current density (J_{sc}), an open-circuit voltage (V_{oc}), a fill factor (FF), and a PCE of 20.98 mA cm^{-2}, 0.95 V, 0.63, and 12.56%, respectively. In Figure S2 (Supporting Information), histograms and standard deviations represent the average photovoltaic performances of 30 devices with ODA-FeS_2 NPs-based HTMs. Photovoltaic parameters of the highest-performing reference cell are displayed in Figure S3 (Supporting Information). The PSCs with ODA-FeS_2 NPs-based HTM exhibited high J_{sc} because of efficient charge extraction, which demonstrates the superior hole transporting ability of HTMs based on ODA-FeS_2 NPs. Furthermore, we measured the hysteresis behavior of the highest-performing cell with ODA-FeS_2 NPs-based HTM, scanning in forward and reverse directions. As shown in Figure S4 (Supporting Information), the best performing solar cells with HTM based on ODA-FeS_2 NPs displays small deviations between the *J–V* curves, scanning opposite directions.

The incident photon-to-current efficiency (IPCE) spectra and integrated photocurrent density were also characterized to confirm the spectral response of the best-performing device with ODA-FeS_2 NPs-based HTM. In Figure 3d, the IPCE spectra

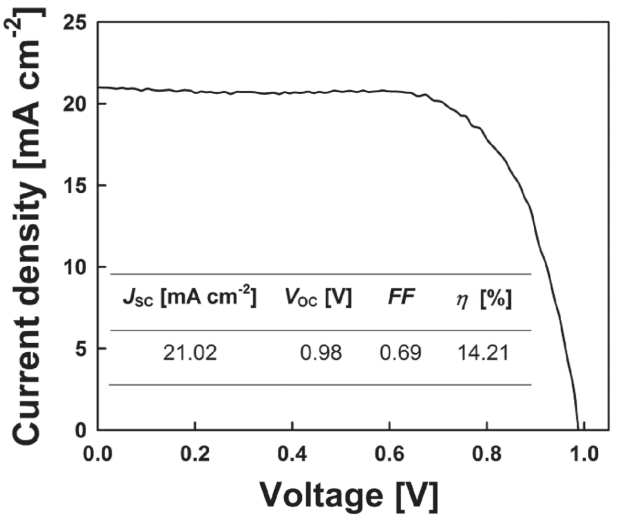

Figure 4. *J–V* curve of the best performing device with bilayered HTM based on spiro-OMeTAD/FeS_2 NPs under 100 mW cm^{-2} illumination (AM 1.5G).

show a broad plateau of >70% over the range 350–750 nm. In addition, the integrated photocurrent density calculated from the IPCE spectra corresponded to that of the J_{sc} value measured from the *J–V* curve. We further investigated the photoluminescence (PL) quenching behavior between perovskite absorber and hole transporting materials to support charge extraction abilities of ODA-FeS_2 NPs based HTMs. As shown in Figure 3e, FeS_2 NPs based HTM shows the dramatic decrease in the PL intensity of perovskite film, which confirms that efficient charge transfer occurred at the ODA-FeS_2 NPs/perovskite interface. Thus, we could confirm that charge extraction abilities of FeS_2 NPs lead to the high J_{sc} of PSCs with ODA-FeS_2 NPs-based HTM.[5,40,41] Based on these results, we verify the highly efficient hole transporting ability of ODA-FeS_2 NPs in PSCs.

Furthermore, in order to compensate the limitation of spiro-OMeTAD and ODA-FeS_2 NPs, we investigated the PSCs with bilayered HTM based on spiro-OMeTAD/ ODA-FeS_2 NPs. **Figure 4** shows the photovoltaic performance of the highest PSC based on bilayerd HTM. The device with bilayered HTM exhibited a J_{sc}, V_{oc}, FF, and a PCE of 21.02 mA cm^{-2}, 0.98 V, 0.69, and 14.21%, respectively. Compared to the pristine ODA-FeS_2 HTM based PSCs, overall photovoltaic properties of the bilayered HTM based device were enhanced. Both J_{sc} and FF were increased since spiro-OMeTAD improved the interface between perovskite layer and FeS_2 NPs. In addition, larger V_{oc} can be attributed to lower the highest occupied molecular orbital (HOMO) energy level of spiro-OMeTAD than that of ODA-FeS_2 NPs. As a result, we confirm that spiro-OMeTAD and ODA-FeS_2 NPs can create a synergy effect on PSCs.

2.4. Long-Term Stability of PSCs with ODA-FeS_2 NPs-Based HTM

Despite its excellent photovoltaic properties, PSCs need to overcome several problems for commercialization. One of the critical problems is that the degradation of $CH_3NH_3PbI_3$ occurs rapidly in humidity.[16] As water encounters $CH_3NH_3PbI_3$, water molecules break the hydrogen bonding between the PbI_3 and CH_3NH_3 units in $CH_3NH_3PbI_3$. The $CH_3NH_3PbI_3$ structure can be completely destroyed because the interaction between the CH_3NH_3 unit and H_2O is much stronger than the bonding between the PbI_3 and CH_3NH_3 units in $CH_3NH_3PbI_3$.[42] As a result, rapid degradation of $CH_3NH_3PbI_3$ produces a drastic decline in the photovoltaic performance.[42–44] Furthermore, toxic PbI_2, a decomposition product, can cause adverse environmental effects.[17] Therefore, a passivation layer is necessary for the underlying perovskite film to increase the stability of perovskite absorber.

In order to prove the moisture-proof ability of ODA-FeS_2 NPs-based HTM, we monitored the long-term stability of PSCs with HTM based on ODA-FeS_2 NPs for 1000 h. For comparison, reference devices with spiro-OMeTAD were also investigated. During the measurement, the photovoltaic performances of the devices were periodically observed at 50% RH and room temperature. All devices were not sealed and have been stored under dark condition. As shown in **Figure 5**a,b, PSCs with spiro-OMeTAD retained only 71% of its initial J_{sc} and 63% of the initial PCE after storage for 1000 h. On the contrary, PSCs with ODA-FeS_2 NPs-based HTM maintained 92% of initial value of J_{sc} and 92% of the initial PCE after 1000 h. PSCs with ODA-FeS_2 NPs-based HTM retained their photovoltaic performance because of the hydrophobicity of ODA-FeS_2 NPs. From these results, we demonstrate the moisture-proof property of ODA-FeS_2 NPs-based HTM for the underlying perovskite absorber and enhanced long-term stability of PSCs.

Besides, the chemical stability of ODA-FeS_2 NPs based HTM with the perovskite layer is essential factor for long-term stability of PSCs because ionic exchange reaction could occur easily between Fe in HTMs and Pb in perovskite absorber. There are several studies to support the ionic exchange reaction between Cu and Pb. Dallago group reported that the addition of cations (Cu^{2+}, Co^{2+}, Al^{3+}, Fe^{3+}, Ni^{2+}, and Cr^{3+}) with Pb complex leads the displacement of lead from complex.[22] In addition, Alivisatos group used cation exchange reactions to solve the limitation of conventional synthesis. Ion exchange reactions give rise to rapid replacement of the cation between various semiconductors.[23,24] Liberato Manna group also demonstrated sequential cation exchange reaction of nanostructures.[25] Therefore, we measured SEM-electron-probe microanalyzer (EPMA) to verify the chemical stability of ODA-FeS_2 NPs with the $CH_3NH_3PbI_3$ absorber. The film composed of FTO glass, TiO_2, $CH_3NH_3PbI_3$, and the ODA-FeS_2 NPs-based layer was stored for 1000 h at room temperature and 50% RH. Figure 5c displays the elemental mappings of Ti (blue pixels), Pb (green pixels), and Fe (red pixels) in the film. A distinct division is observed between Pb and Fe in the elemental mappings. The obvious distinction indicates that the long alkyl chain of ODA prevented the ionic exchange between the Fe in the HTM layer and the Pb in the perovskite absorbers. A small amount of elemental Pb is observed under FTO/glass because ion beam focusing dissolved Pb cations from the $CH_3NH_3PbI_3$.[21] Furthermore, we also analyzed the ionic exchange behavior between Fe in pristine FeS_2

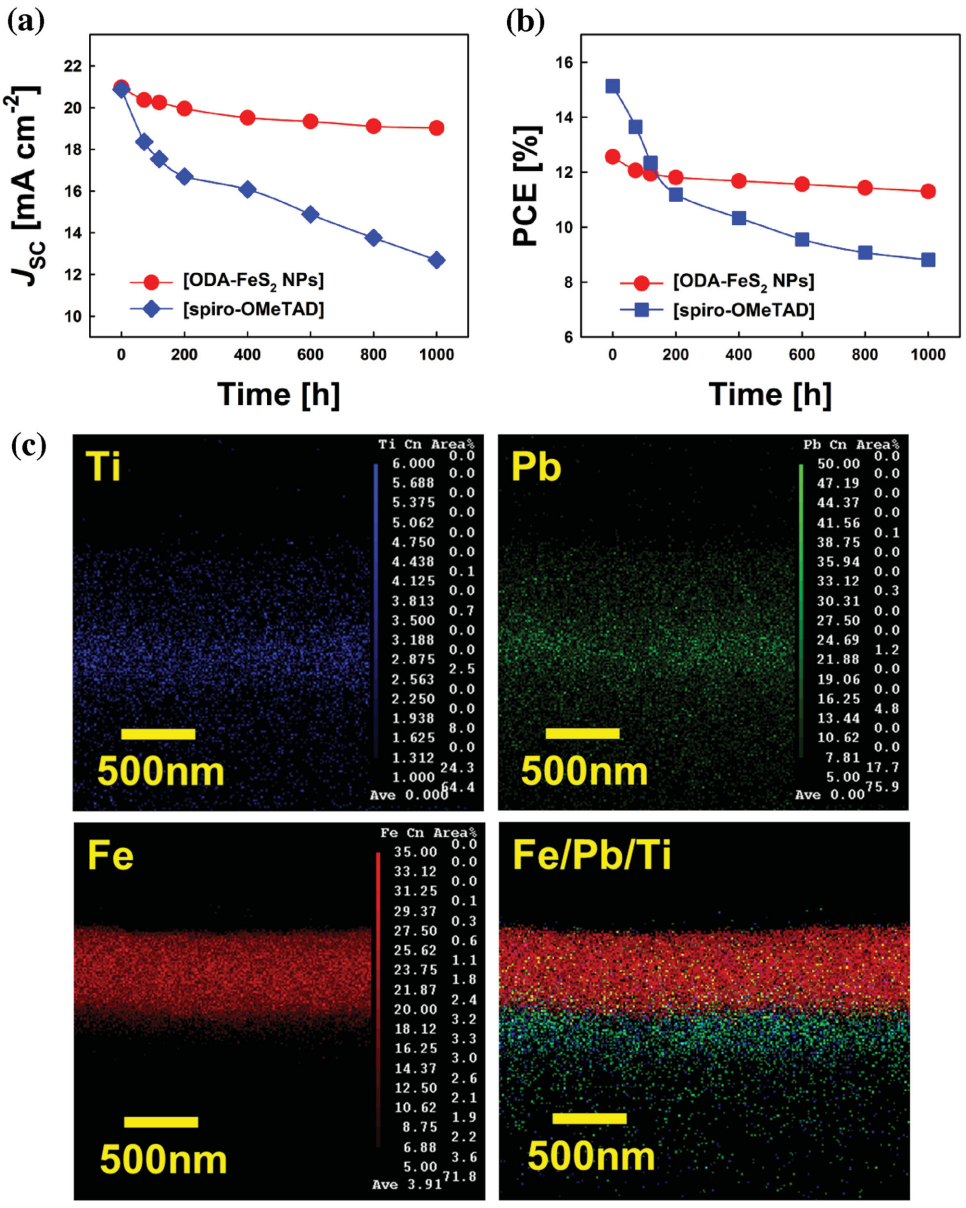

Figure 5. Long-term stability of the PSCs with ODA-FeS_2 NPs-based HTM (red circle) and spiro-OMeTAD (blue tetragon) for 1000 h a) short-circuit current density and b) efficiency of the highest-performing cells with different HTMs c) SEM-EPMA mappings of titanium (blue pixels), lead (green pixels), iron (red pixels), and total elements in the film composed of TiO_2/$CH_3NH_3PbI_3$/ODA-FeS_2 NPs.

film (without ODA ligand) and Pb in the perovskite layer. As shown in Figure S5a (Supporting Information), spatial separation between two layers became ambiguous because cation exchange occurred between Fe in pristine FeS_2 film and Pb in perovskite layer. As a result, Fe ions migrated to perovskite layer and Pb ions moved to FeS_2 layer. On the contrary, Figure S5b (Supporting Information) indicated a remarkable distinction in the elemental mappings of Fe in ODA capped FeS_2 NPs based film and Pb in perovskite layer. Therefore, we demonstrated that ODA ligand could prevent the ionic exchange between Fe in HTM and Pb in perovskite layer efficiently. These results confirm that ODA-FeS_2 NPs contribute to the long-term stability of PSCs.

3. Conclusion

In summary, we prove that the ODA-FeS_2 NPs exhibited excellent performance in hole extraction and efficiently prevented moisture attack on the perovskite absorbers. Through the hot injection method, FeS_2 nanostructures could be precisely synthesized at high concentrations. Even when the FeS_2 NPs were modified by long alkyl ligands, the ionic conductivity of ODA-FeS_2 nanostructured thin film was one order of magnitude higher than that of the pristine spiro-OMeTAD. Furthermore, ODA-FeS_2 NPs-based films are more hydrophobic than the spiro-OMeTAD. These results demonstrate that FeS_2 NPs could act as an efficient bi-functional layer in PSCs. Therefore,

ODA-FeS_2 NPs-based HTM are potentially promising materials and can help in realizing highly robust PSCs.

4. Experimental Section

Materials: Iron (II) chloride tetrahydrate ($FeCl_2{\cdot}4H_2O$, 99%), octadecylamine ($CH_3(CH_2)_{16}CH_2NH_2$, 97%), diphenylether ($(C_6H_5)_2O$, 99%), lead (II) iodide (PbI_2, 99.9%), dimethyl sulfoxide (DMSO), *N,N*-dimethylformamide (DMF), anhydrous chloroform (99%), and ethanol (99%) were purchased from Sigma-Aldrich. Methylammonium iodide (CH_3NH_3I) was purchased from Dyesol. All chemicals were used as received without any further purification.

Synthesis of ODA-FeS_2 NPs: ODA-FeS_2 NPs were synthesized using a modified hot injection method proposed by Puthussery et al.[28] First, 0.8 mmol of $FeCl_2{\cdot}4H_2O$ was dissolved in 0.15 mol ODA. The mixed solution was placed in a three-neck flask and de-aerated by bubbling 99.99% nitrogen (N_2) gas for 60 min. An injection solution was obtained by the dissolution of 4 mmol of sulfur in 10 mL of diphenyl ether under N_2 atmosphere. The injection solution was added dropwise into the solution ($FeCl_2{\cdot}4H_2O$ in ODA) while stirring and continuously purging the reaction media with N_2 gas for 30 min. After the reaction mixture was brought to boiling temperature, ODA-FeS_2 NPs were initially formed, and color of the solution changed from brown to black. The ODA-FeS_2 NPs were allowed to crystallize and grow under conditions of continuous reflux at 220 °C for 5–300 min. The reaction time determined the diameter of the resulting NPs. The as-grown ODA-FeS_2 NPs were further purified by washing with ethanol, ethanol/chloroform (10:1), and methanol/chloroform (10:1), respectively. Any residual side products from the NPs suspension were removed by centrifugation at 3500 rpm for 10 min. The final products were dissolved in chloroform. The resulting ODA-FeS_2 NPs solution had high solubility and purity, which is required for the deposition of the ODA-FeS_2 NPs-based thin films.

Characterization of ODA-FeS_2 NPs: ODA-FeS_2 NPs were examined by TEM (FEI, TECNAI G^2 F30 ST, at 100 kV). The crystal structure of ODA-FeS_2 NPs was analyzed using an X-ray diffractometer (Rigaku, DMAX-2500/PC) operating at 20 kV and 200 mA with a rotating anode and Cu Kα radiation (λ = 0.15418 nm). (XPS was used to determine the binding state of Fe and S ion using an AXIS-HIS spectrometer with monochromatic Al Kα radiation (1486.3 eV). XPS data were acquired over the range 0–1400 eV with a constant pass energy of 117.4 eV at the nominal photoelectron takeoff angle of 45°. The wettability of ODA-FeS_2 nanostructured film and spiro-OMeTAD was analyzed by the static contact angle method. Water droplets were deposited onto both ODA-FeS_2 NPs-based film and spiro-OMeTAD using a micro-syringe. Then, the water contact angle was measured. Conductivities of ODA-FeS_2 NPs and spiro-OMeTAD were measured by the four-pin probe system (MCP-HT610, LORESTA-GP). Silver electrodes, 50 μm apart, were deposited on the films for measurement. The surface image of the film based on ODA-FeS_2 NPs was investigated by high-resolution SEM (JXA-8100, JEOL). Topographical mapping for surface morphology and roughness of the ODA-FeS_2 NPs-based films was performed using AFM (Park system, XE-100) via the tapping mode with an Al-coated cantilever. In addition, conductive atomic force microscopy (C-AFM, Park system, XE-100) with a Pt-coated cantilever was used to investigate the charge transport properties of the film at the micrometer scale.

To investigate the hole mobility of FeS_2 NPs based films and pristine FeS_2 bulk film, all of the samples were prepared on Si substrates (1.5 cm × 1.5 cm). A 150 nm thick ODA-FeS2 NPs based film was deposited on the substrates using spray-coating. To compare the hole mobility of pristine FeS_2 bulk film, ODA-FeS_2 NPs coated Si substrates were annealed in a sulfur atmosphere for 2 h to eliminate ODA ligand. 100 μm thick Ag top electrodes were deposited on the corner of FeS_2 NPs based films and pristine FeS_2 bulk film, respectively. The hole mobility measurement of the FeS_2 NPs based layer and pristine FeS_2 bulk film were studied by a hole effect system (HL5500PC).

Device Fabrication: Patterned FTO glasses were washed with acetone, ethanol, and 2-propanol using sonication. The compact TiO_2 blocking layer was spin-coated on the FTO substrates and sintered at 500 °C for 30 min. For preparing the mesoporous TiO_2 layer, the TiO_2 paste (consisting of TiO_2, ethyl cellulose, lauric acid, and terpineol) was mixed with ethanol (TiO_2 to ethanol weight ratio of 2:8). After mixing, the TiO_2 solution was deposited by spin-coating at 5000 rpm for 60 s and then annealed at 500 °C in air. After that, a highly dense $CH_3NH_3PbI_3$ film was formed by a modified procedure.[8] 1 mmol PbI_2, 1 mmol CH_3NH_3I, and 1 mmol DMSO were dissolved in DMF and stirred at 70 °C. The dissolved solution was spin-coated on the mesoporous TiO_2 film at 4000 rpm for 30 s, and then, diethyl ether was added dropwise on the rotating film. After spinning, the $CH_3NH_3PbI_3$ film was dried at 100 °C for 20 min and cooled to 25 °C. The ODA-FeS_2 NPs solution (5 mg mL^{-1}) was deposited onto the $TiO_2/CH_3NH_3PbI_3$ substrate using a spray-coating method with N_2 carrier gas.[45] The resultant film was thermally annealed at 70 °C for 2 min in air. After thermal annealing, a 100 nm thick Au electrode was thermally evaporated on top of the device to form the back contact (see Figure S1, Supporting Information).

Characterization of Solar Cells: The cross-sectional image of the prepared device was characterized by high-resolution SEM (JXA-8100, JEOL) and the elemental mapping of the film composed of FTO glass, TiO_2, $CH_3NH_3PbI_3$, and ODA-FeS_2 NPs was performed using an SEM-EPMA (JXA-8100F, JEOL). The current density–voltage (*J–V*) properties of the perovskite solar cells were characterized using a Keithley 2400 source meter with a 1600 W solar simulator (Yamashita Denso Corp., YSS-200A). A xenon lamp equipped with a KG-3 filter served as the light source. A reference Si solar cell was used to adjust the light intensity to 1 sun condition (AM 1.5G and 100 mW cm^{-2}). The active area was measured using a digital microscope camera (Moticam1000). An IPCE system (PV Measurements Inc.) was used to measure the external quantum efficiency (EQE). For precise measurements, metal aperture masks were attached on each cell to define the active area. The steady-state PL spectra of the bare perovskite absorber, perovskite absorber/ODA-FeS_2 film, and perovskite absorber/spiro-OMeTAD were measured by excitation at 550 nm using a Fluorolog3 photoluminescence spectrometer system with a monochromator (iHR320, HORIBA Scientific).

Supporting Information

Supporting Information is available from the Wiley Online Library or from the author.

Acknowledgements

B. Koo and H. Jung contributed equally to this work. This work was supported from the Technology Development Program to Solve Climate Changes (2015M1A2A2056824) and the Global Frontier R&D Program on Center for Multiscale Energy System (2012M3A6A7054856), and 2014 University-Institute cooperation program funded by the National Research Foundation under the Ministry of Science, ICT & Future Planning, Korea. This work was also supported by the KIST institutional programs.

Received: March 3, 2016
Revised: April 15, 2016
Published online: June 9, 2016

[1] Z. Xiao, Q. Dong, C. Bi, Y. Shao, Y. Yuan, J. Huang, *Adv. Mater.* **2014**, *26*, 6503.
[2] J.-Y. Jeng, Y.-F. Chiang, M.-H. Lee, S.-R. Peng, T.-F. Guo, P. Chen, T.-C. Wen, *Adv. Mater.* **2013**, *25*, 3727.
[3] W. Zhang, M. Saliba, S. D. Stranks, Y. Sun, X. Shi, U. Wiesner, H. J. Snaith, *Nano Lett.* **2013**, *13*, 4505.

[4] Z. Xiao, C. Bi, Y. Shao, Q. Dong, Q. Wang, Y. Yuan, C. Wang, Y. Gao, J. Huang, *Energy Environ. Sci.* **2014**, *7*, 2619.
[5] P. Docampo, J. M. Ball, M. Darwich, G. E. Eperon, H. J. Snaith, *Nat. Commun.* **2014**, *4*, 2761.
[6] A. Kojima, K. Teshima, Y. Shirai, T. Miyasaka, *J. Am. Chem. Soc.* **2009**, *13*, 6050.
[7] J.-H. Im, C.-R. Lee, J.-W. Lee, S.-W. Park, N.-G. Park, *Nanoscale* **2011**, *3*, 4088.
[8] N. Ahn, D.-Y. Son, I.-H. Jang, S. M. Kang, M. Choi, N.-G. Park, *J. Am. Chem. Soc.* **2015**, *137*, 8696.
[9] J. T.-W. Wang, J. M. Ball, E. M. Barea, A. Abate, J. A. Alexander-Webber, J. Huang, M. Saliba, I. Mora-Sero, J. Bisquert, H. J. Snaith, *Nano Lett.* **2014**, *14*, 724.
[10] J.-H. Im, I.-H. Jang, N. Pellet, M. Gratzel, N.-G. Park, *Nat. Nanotechnol.* **2014**, *9*, 927.
[11] H. Zhou, Q. Chen, G. Li, S. Luo, T. Song, H.-S. Duan, Z. Hong, J. You, Y. Liu, Y. Yang, *Science* **2014**, *345*, 542.
[12] G. E. Eperon, V. M. Burlakov, P. Docampo, A. Goriely, H. J. Snaith, *Adv. Funct. Mater.* **2014**, *24*, 151.
[13] Best solar cell efficiencies chart. www.nrel.gov/ncpv/images/efficiency_chart.jpg (accessed: January 2016).
[14] K. Zhang, L. Wang, Y. Liang, S. Yang, J. Liang, F. Cheng, J. Chen, *Synth. Met.* **2012**, *162*, 490.
[15] Q. Luo, Y. Zhang, C. Liu, J. Li, N. Wang, H. Lin, *J. Mater. Chem. A* **2015**, *3*, 15996.
[16] J. Yang, B. D. Siempelkamp, D. Liu, T. L. Kelly, *ACS Nano* **2015**, *9*, 1955.
[17] M. Gratzel, *Nat. Mater.* **2014**, *13*, 838.
[18] B. O'Regan, F. Lenzmann, R. Muis, J. Wienke, *Chem. Mater.* **2002**, *14*, 5023.
[19] M. N. Amalina, A. A. E. Najwa, M. H. Abdullah, M. Z. Musa, M. Rusop, *IOP Conf. Ser.: Mater. Sci. Eng.* **2013**, *46*, 012012.
[20] J. A. Christians, R. C. M. Fung, P. V. Kamat, *J. Am. Chem. Soc.* **2014**, *136*, 758.
[21] P. Qin, S. Tanaka, S. Ito, N. Tetreault, K. Manabe, H. Nishino, M. K. Nazeeruddin, M. Gratzel, *Nat. Commun.* **2014**, *5*, 3834.
[22] A. Smaniottoa, A. Antunes, I. d. N. Filho, L. D. Venquiaruto, D. d. Oliveira, A. Mossi, M. D. Luccio, H. Treichel, R. Dallago, *J. Hazard. Mater.* **2009**, *172*, 1677.
[23] B. J. Beberwyck, A. P. Alivisatos, *J. Am. Chem. Soc.* **2012**, *134*, 19977.
[24] J. M. Luther, H. Zheng, B. Sadtler, A. P. Alivisatos, *J. Am. Chem. Soc.* **2009**, *131*, 16851.
[25] H. Li, M. Zanella, A. Genovese, M. Povia, A. Falqui, C. Giannini, L. Manna, *Nano Lett.* **2011**, *11*, 4964.
[26] A. Ennaoui, S. Fiechter, H. Goslowsky, H. Tributsch, *J. Electrochem. Soc.* **1985**, *132*, 1579.
[27] A. Ennaoui, S. Fiechter, Ch. Pettenkofer, N. Alonso-Vante, K. Buker, M. Bronold, Ch. Hopfner, H. Tributsch, *Sol. Energy Mater. Sol. Cells* **1993**, *29*, 289.
[28] J. Puthussery, S. Seefeld, N. Berry, M. Gibbs, M. Law, *J. Am. Chem. Soc.* **2011**, *133*, 716.
[29] S. Shukla, N. H. Loc, P. P. Boix, T. M. Koh, R. R. Prabhakar, H. K. Mulmudi, J. Zhang, S. Chen, C. F. Ng, C. H. A. Huan, N. Mathews, T. Sritharan, Q. Xiong, *ACS Nano* **2014**, *8*, 10597.
[30] D.-Y. Wang, Y.-T. Jiang, C.-C. Lin, S.-S. Li, Y.-T. Wang, C.-C. Chen, C.-W. Chen, *Adv. Mater.* **2012**, *24*, 3415.
[31] M. Nam, D. Choi, S. Kim, S. Lee, K. Lee, S. Kim, *J. Mater. Chem. A* **2014**, *2*, 9758.
[32] Y. Ko, H. Baek, Y. Kim, M. Yoon, J. Cho, *ACS Nano* **2012**, *7*, 143.
[33] L. Xu, R. G. Karunakaran, J. Guo, S. Yang, *ACS Appl. Mater. Interfaces* **2012**, *4*, 1118.
[34] D. Ebert, B. Bhushan, *Langmuir* **2012**, *28*, 11391.
[35] R. G. Karunakaran, C.-H. Lu, Z. Zhang, S. Yang, *Langmuir* **2011**, *27*, 4594.
[36] X. Chen, Z. Wang, X. Wang, J. Wan, J. Liu, Y. Qian, *Inorg. Chem.* **2005**, *44*, 951.
[37] X. Qiu, M. Liu, T. Hayashi, M. Miyauchi, K. Hashimoto, *Chem. Commun.* **2013**, *49*, 1232.
[38] C. Wadia, Y. Wu, S. Gul, S. K. Volkman, J. Guo, A. P. Alivisatos, *Chem. Mater.* **2009**, *21*, 2568.
[39] H. Zhou, Y. Zhang, C. Mai, S. D. Collins, T. Nguyen, G. C. Bazan, A. J. Heeger, *Adv. Mater.* **2013**, *26*, 780.
[40] B. Conings, L. Baeten, C. De Dobbelaere, J. D'Haen, J. Manca, H. G. Boyen, *Adv. Mater.* **2014**, *26*, 2041.
[41] K.-C. Wang, J.-Y. Jeng, P.-S. Shen, Y.-C. Chang, E. W.-G. Diau, C.-H. Tsai, T.-Y. Chao, H.-C. Hsu, P.-Y. Lin, P. Chen, T.-F. Guo, T.-C. Wen, *Sci. Rep.* **2014**, *4*, 4756.
[42] X. Dong, X. Fang, M. Lv, B. Lin, S. Zhang, J. Ding, N. Yuan, *J. Mater. Chem.* **2015**, *3*, 5360.
[43] Y. Zhao, K. Zhu, *Chem. Commun.* **2014**, *50*, 1605.
[44] J. A. Christians, P. A. M. Herrera, P. V. Kamat, *J. Am. Chem. Soc.* **2015**, *137*, 1530.
[45] I. Jeong, J. Lee, K. L. V. Joseph, H. Lee, J. Kima, S. Yoon, J. Lee, *Nano Energy* **2014**, *9*, 392.